npj | 2D materials and applications

www.nature.com/npj2dmaterials

ARTICLE OPEN

Check for updates

Raman enhancement induced by exciton hybridization in molecules and 2D materials

Hikari Kitadai[1], Qishuo Tan[1], Lu Ping[2] and Xi Ling[1,2,3]✉

Surface-enhanced Raman spectroscopy (SERS) is a powerful technique for trace-level fingerprinting. Recently, layered two-dimensional (2D) materials have gained significant interest as SERS substrates for providing stable, uniform, and reproducible Raman enhancement with the potential for trace-level detection. Yet, the development of effective 2D SERS substrates is still hindered by the lack of fundamental understanding of the coupling mechanism between target molecules and substrates. Here, we report a systematic excitation-dependent Raman spectroscopy investigation on the coupling between 2D materials such as SnS_2, MoS_2, WSe_2, and graphene and small organic molecules like rhodamine 6G (Rh 6G). Strong coupling between SnS_2 and Rh 6G is found due to their degenerate excitons through Raman excitation profiles (REP), leading to the enhancement of Rh 6G vibrational modes that are observable down to 10^{-13} M. Our study shows that exciton coupling in the substrate-adsorbate complex plays a vital role in the Raman enhancement effect, opening a new route for designing SERS substrates for high sensitivity.

npj 2D Materials and Applications (2024)8:11 ; https://doi.org/10.1038/s41699-024-00446-z

INTRODUCTION

The discovery of the graphene-enhanced Raman scattering (GERS) effect early in 2010 paved the way for the study of Raman enhancement on two-dimensional (2D) materials[1]. Since then, the Raman enhancement effect has been observed on several other layered 2D materials, including boron nitride[2,3], black phosphorus[4], transition metal dichalcogenides (TMDs)[5,6], metal-carbides (MXenes)[7], among others[8,9]. In contrast to traditional noble-metal SERS substrates, the enhanced Raman scattering effect on 2D materials is ascribed to increased molecular polarizability arising from electronic couplings between the adsorbate and the substrate (chemical enhancement mechanism – CM) rather than the plasmonic effect (electromagnetic enhancement mechanism – EM)[10–12]. The atomically flat and chemically inert surfaces and tunable electronic properties of 2D materials make them ideal platforms for investigating the effects of electronic couplings on the Raman enhancement, which ultimately offers insight into the enhancement mechanism between the organic molecules and inorganic semiconductors. Notably, in the leading theory of SERS on semiconductors described by Lombardi and Birke and their co-workers, strong Raman intensities are expected when the excitation energy coincides with either a charge-transfer transition (μ_{CT}), molecular absorption (μ_{mol}), or exciton resonance (μ_{exc})[12]. Additional enhancements may be possible by achieving multiple resonances with the same excitation source[13]. While most enhancement observations on 2D materials have been ascribed to charge-transfer resonances, very few studies have focused on the effect of achieving dual resonances in the system. Some reports have hinted at the potential for improving Raman enhancement by aligning exciton resonances to charge transfer resonances[14,15], yet a systematic study into aligning exciton resonances to molecular resonances remain under-explored[16]. Our research presents a systematic study into Raman enhancement by exciton hybridization by probing different μ_{mol} and μ_{exc} alignments, offering new insights in designing semiconductor-based SERS substrates for trace-level chemical sensing.

In this work, we explore this co-resonance effect on Raman enhancement by selecting an appropriate system in which resonance with both molecule (μ_{mol}) and 2D material ($\mu_{2D\ mat}$) are achieved with the same excitation energy. Recently, 2D SnS_2 has garnered newfound interest in light-harvesting applications due to its high carrier mobility[17,18], ranging from photocatalysis[19], photodetectors[20,21], to dye-sensitized solar cells[22,23]. So far, the application of SnS_2 as a SERS substrate is still under-explored[5,24–26], despite its chemical stability, non-toxicity, and earth abundance[27]. Here, we showcase 2D SnS_2 and rhodamine 6G (Rh 6G) as a model platform for investigating the effects of simultaneously achieving μ_{mol} and $\mu_{2D\ mat}$ resonances in the molecule-substrate complex[12,13,28–30], Fig. 1a, and its potential for trace-level sensing; structures are shown in Supplementary Fig. 1. 2H-SnS_2 is an n-type semiconductor with a bandgap around 2.2–2.4 eV[31–35] (μ_{exc} ~ 2.3 eV) and Rh 6G has an S_0-S_0 transition at 532 nm[36] (μ_{mol} ~ 2.3 eV). Moreover, Rh 6G has a large Raman cross-section[37], which allows Raman spectra to be acquired even under off-resonance condition. A comprehensive investigation using excitation-wavelength dependent Raman measurements reveal exciton hybridization between SnS_2 and Rh 6G, leading to a limit of detection (LOD) of 10^{-13} M. This phenomenon is further supported by tuning the μ_{mol} and μ_{exc} alignments and measuring excitation-wavelength dependent Raman spectra for Rh 6G adsorbed on MoS_2, WSe_2, and graphene, as well as for Rhodamine B (Rh B) and Rhodamine 123 (Rh 123) adsorbed on SnS_2.

RESULTS

Characterization of Rh 6G Raman enhancement on SnS_2

The SERS spectrum of Rh 6G (10^{-5} M) adsorbed on mechanically exfoliated few-layer SnS_2 crystal is shown in Fig. 1b. In addition to the SnS_2 A_{1g} mode at 313 cm^{-1} and the Si peaks at 520.7 and ~950 cm^{-1}, 15 characteristic Rh 6G peaks are observed. Their

[1]Department of Chemistry, Boston University, Boston, MA 02215, USA. [2]Division of Materials Science and Engineering, Boston University, Boston, MA 02215, USA. [3]The Photonics Center, Boston University, Boston, MA 02215, USA. ✉email: xiling@bu.edu

frequency and vibrational assignments are summarized in Supplementary Table 1. Resonance Raman (RR) spectra, especially when obtained by irradiating into a strong absorption band like the $S_{0,0}$-$S_{1,0}$ transition in Rh 6G, is largely influenced by Franck-Condon overlap integrals[38,39]. These integrals contribute to the intensity of a given normal only when there is a difference in the potential energy surfaces between the ground and excited electronic states. This difference in potential surfaces is evident if the bond distances between the two states involved in the transition are not the same, such as in carbon-bond stretching modes[36,40]. In aromatic molecules like Rh 6G, this difference in bond distance is typically observed for C–C bonds[41]. Consequently, it is anticipated that stretching modes associated with the carbon skeleton will result in the most intense RR bands, and is in agreement with previous experimental reports[36,42–44].

Moreover, under resonant conditions, it is interesting to note that the C–C bending modes, i.e., 613 cm^{-1}, greatly intensify when compared to off-resonance conditions. This is intriguing because, typically, vibrations of this nature do not undergo marked changes upon electronic shifts. This implies that the intensification of the 613 cm^{-1} mode arises from another source, namely Herzberg-Teller vibronic coupling, a mechanism well-documented in resonance Raman spectroscopy[45]. In our research, the C–C in-plane bending mode at 613 cm^{-1} is the most pronounced feature when Rh 6G is deposited on SnS_2 under resonance, displaying an intensity about 3 times stronger than that of the 1361 cm^{-1} mode. This mode-selective enhancement emphasizes the contribution of vibronic coupling to the SERS spectrum, which is central to the CM theory. Furthermore, we believe the unusually strong 613 cm^{-1} mode serves as indication of the efficient vibronic coupling in the Rh 6G/SnS_2 system, given the vibronic coupling dependence of this mode[36].

We further investigated the SERS sensitivity of SnS_2 by immersion in dilute solutions of Rh 6G with the concentration ranging from 10^{-14} to 10^{-4} M as shown in Fig. 1c and Supplementary Fig. 2. At higher concentrations, two characteristic Rh 6G Raman peaks at 613 and 774 cm^{-1} are observed. Their intensities gradually decrease until only the 613 cm^{-1} mode is present at 10^{-13} M, which is the LOD we achieved. Supplementary Table 2 presents the LOD for Rhodamine 6G (Rh 6G) adsorbed onto various 2D SERS systems. These systems include semiconducting, metallic, and doped 2D materials. Currently, SnS_2 stands out as the most sensitive pristine 2D semiconductor SERS substrate for Rh 6G detection. However, we do note metallic 2D substrates (e.g., TaS_2, $NbSe_2$, and 1T′ WSe_2) tend to exhibit superior LOD, suggesting they may rely on a distinct enhancement mechanism. Nevertheless, the LOD for Rh 6G on SnS_2 is very promising, on par with the most sensitive reports so far[44,46,47], and even rivals plasmon-based SERS substrates[48,49] .

It has been widely reported in the field of Raman enhancement effect on 2D crystals that few-layered samples offer the highest enhancement factors when compared to their bulk counterpart[5,11,16], due to increased light absorption by the underlying substrate. This phenomenon is also observed in our study: Supplementary Fig. 3 shows the spectra for Rh 6G adsorbed on different number of layers which are confirmed by atomic force microscopy (AFM) (Supplementary Fig. 4). For instance, the 613 cm^{-1} mode intensity is about 10 times stronger for a 3L sample than that for an 18L sample. This behavior highlights the thickness-dependent Raman enhancement effect on SnS_2 is likely due to optical absorption by the substrate and the layer-dependent electronic band structure[50]. Supplementary Fig. 5 plots the 613 cm^{-1} peak intensity as a function of concentration for Rh 6G adsorbed on 3, 11, and 18L SnS_2 samples. At the lower concentration regime, the Rh 6G Raman intensity is notably low. As the concentration increases, there is a pronounced amplification in the Raman intensity, resulting from more Rh 6G interacting with the SnS_2 substrate. At even higher concentrations, the Raman intensity reaches a plateau, which is particularly obvious for the 18L sample. This plateau suggests a saturation point where increasing the sample concentration further doesn't result in a proportional increase in Raman intensity, which is attributed to the "first-layer effect"[51]. Nevertheless, the LOD for Rh 6G on 3L and 18L SnS_2 is the same and shows that trace-level detection is consistent even for multilayered samples.

To better understand the Raman enhancement mechanism of Rh 6G on SnS_2 we measured absorption spectra of liquid exfoliated SnS_2 mixed with Rh 6G to probe whether their coupling gives rise to new optical transitions. Figure 1d shows the absorption spectra of Rh 6G when dissolved in two distinct solutions with various concentrations from 30 to 377 nM: one comprising solely of isopropyl alcohol (IPA) and another made of SnS_2 dispersed in IPA. In the case of Rh 6G dissolved in pure IPA (bottom spectra), the absorption baseline starts at zero. These spectra display two distinct peaks corresponding to the $S_{0,0}$-$S_{1,0}$ transition at 532 nm (2.33 eV) with a vibronic shoulder, $S_{0,0}$-$S_{1,1}$, at 508 nm (2.44 eV). These transitions are characteristic of Rh 6G and provide a clear benchmark for its identification and characterization.

Turning our attention to the absorption spectra of SnS_2 (top spectra), there is a noticeable broad background. Interestingly, this background initiates at an absorption baseline that is elevated by about 0.1 units in comparison to the IPA solution. This difference in baseline is an important consideration and is indicative of SnS_2's inherent optical properties. In the mixture of Rh 6G and SnS_2, the absorption baseline decreases from 0.1 unit with increasing Rh 6G concentration. Additionally, the two peaks at 2.33 eV and 2.44 eV are evidence of the presence of Rh 6G in the mixed solution. An intriguing feature is the presence of isosbestic points at 511 nm and 547 nm in the Rh 6G/SnS_2 mixtures. Isosbestic points, often observed in absorption spectroscopy, mark a consistent molar absorptivity between two species at specific wavelengths, despite changes in concentrations[52]. In this context, the isosbestic points may serve as evidence for the interaction between Rh6G and SnS_2[53]. We also performed the micro-absorption spectra of dried SnS_2 flakes before and after Rh 6G deposition (Supplementary Fig. 6) (from where we obtain the difference spectra by subtracting the Rh 6G/SnS_2 absorption spectrum from pristine SnS_2,) which appear featureless.

Raman excitation profiles of Rh 6G/SnS_2 and the exciton hybridization mechanism

While conventional absorption spectroscopy did not yield valuable information about the potential coupling between SnS_2 and Rh 6G, we further performed excitation-dependent Raman spectroscopy measurements, from which Raman excitation profiles (REPs) are obtained. REPs were reported particularly useful in probing the coupling in semiconductor-based SERS substrates because the excitation energies at which resonances occur can be traced to electronic transitions in the complex[10,37,54]. Here, we obtain and compare the REPs of Rh 6G on several different 2D crystals, including MoS_2, WSe_2, and graphene, as well as for Rh B and Rh 123 adsorbed on SnS_2. In this work, all REPs were collected with 11 laser lines ranging from 648 to 458 nm (1.91 to 2.70 eV). Figure 2a shows the typical Raman spectra of Rh 6G (10^{-5} M) adsorbed on SnS_2 under 11 laser excitations. It is clear that the Raman peaks of Rh 6G are strongest when excited under 2.3–2.6 eV lasers and quickly decrease outside this window. Additionally, the relative peak intensities vary in this resonance window. For example, at 2.33 eV, the 613 cm^{-1} mode is significantly stronger than the xanthene ring modes in the range of 1350–1650 cm^{-1}. However, at 2.54 eV, the 613 cm^{-1} mode is much weaker. We also note that because of the strong Rh 6G emission, the spectra acquired with 2.33 eV excitation are noisier.

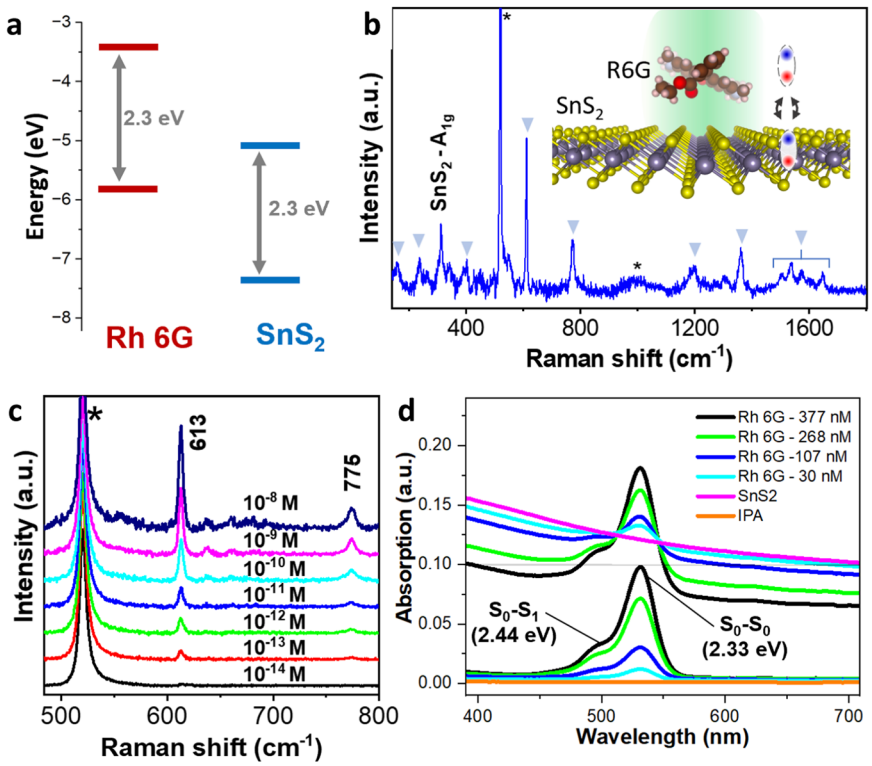

Fig. 1 Characterization of Rh 6G Raman enhancement on SnS_2. **a** Energy band alignment for Rh 6G and SnS_2. **b** Raman spectrum of Rh 6G on SnS_2 excited with 2.33 eV; peaks with an asterisk are from the Si substrate. Inset shows schematics for Rh 6G/SnS_2 and their coupling through exciton alignment. **c** Concentration-dependent Raman spectra of Rh 6G on a 3L SnS_2 sample, with 2.33 eV excitation. Spectra shown were baseline corrected for photoluminescence background. **d** Comparison of absorption spectra for Rh 6G with various concentrations dissolved in IPA (bottom spectra), and dissolved in SnS_2 solution (top spectra).

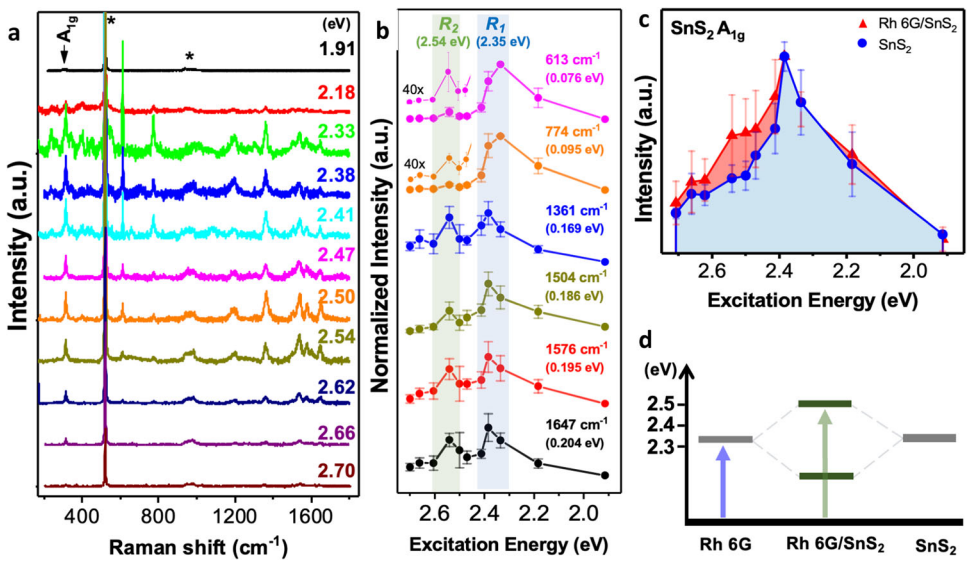

Fig. 2 Raman excitation profiles for Rh 6G/SnS_2. **a** Rh 6G/SnS_2 Raman spectra under different excitation energies, from 1.91 to 2.70 eV. Peaks marked with an asterisk are from the Si substrate; the A_{1g} peak is from the SnS_2. **b** Raman excitation profiles for selected Rh 6G vibrational modes. Blue shaded area marks the R_1 resonance peak at 2.35 eV, and in green the R_2 resonance peak at 2.54 eV. Inset shows the zoomed in R_2 region for the 613 and 774 cm^{-1} bands. **c** REPs of the A_{1g} mode of SnS_2 before and after Rh 6G deposition. **d** Proposed exciton hybridization between Rh 6G and SnS_2, depicting the new resonant energies. Error bars in (**b**) and (**c**) represent the standard deviation from measuring multiple samples.

We further plot the REPs for different Rh 6G modes in Fig. 2b. The REP intensities are calibrated to a quartz reference and normalized for easier visualization. It is clearly seen that all Rh 6G modes display a resonance peak at ~2.35 eV (R_1) in the REPs, matching well with the $S_{0,0}$-$S_{1,0}$ absorption of Rh 6G at 2.33 eV[37,54]. We note the resonance maximum for the bending modes (613, 774 cm^{-1}) occur at 2.33 eV, whereas for the xanthene ring modes (those above 1350 cm^{-1}), the maxima occur at 2.38 eV. This slight

difference in resonance underscores the vibronic character of the bending modes[37,43,55], as well as a possible contribution from conformational distortion of the xanthene core upon Rh 6G chemisorption[36] on SnS_2. Moreover, an additional resonance peak at 2.54 eV (R_2) is also observed for all modes and is strongest for the xanthene ring. We note the relative intensity between R_2 and R_1 varies depending on the vibrational modes. For example, R_2 is as intense as R_1 for the 1361 cm^{-1} mode, whereas R_2 is weaker than R_1 for the 1504 cm^{-1} mode. While it is clear that R_1 matches well with the μ_{Rh6G}, the origin of R_2 at 2.54 eV requires further analysis.

We verify R_2 is a feature of the Rh 6G/SnS_2 complex and not the underlying SnS_2 substrate by comparing the REP for the SnS_2 A_{1g} mode before and after deposition of Rh 6G, as shown in Fig. 2c. For intrinsic SnS_2 sample without Rh 6G deposited, the REP displays a single maximum at 2.38 eV, suggesting a transition at this energy, matching well with the $S_{0,0}$-$S_{1,0}$ transition in Rh 6G at 2.33 eV. However, the A_{1g} REP shows increased Raman activity at ~2.54 eV after Rh 6G deposition, which is at the same energy as R_2, suggesting a synergistic effect between Rh 6G and SnS_2. Recently, Muccianti et al. proposed an exciton hybridization concept for the Raman enhancement of 3,4,9,10-tetracarboxylic dianhydride (PTCDA) when adsorbed on WSe_2[16]. The authors argued that hybridization of degenerate excitons in PTCDA and WSe_2 led to the formation of new exciton states with different resonant energies. We believe a similar concept applies to the coupling between Rh 6G and SnS_2: degenerate excitons from the molecule (μ_{Rh6G}) and the substrate (μ_{SnS_2}) couple and hybridize, giving rise to excitons with new resonant energies, as shown in Fig. 2d. The R_2 (2.54 eV) resonance peak likely stems from the hybridization of the degenerate Rh 6G $S_{0,0}$-$S_{1,0}$ transition and the SnS_2 exciton transition (green arrow in Fig. 2d), while the R_1 resonance peak stems from the Rh 6G $S_{0,0}$-$S_{1,0}$ transition (blue arrow in Fig. 2d). In the following, we further discuss other possible origins for R_2 including light scattering resonance, charge-transfer resonance, and electronic hybridizations.

Investigation of the resonance peaks

First, we consider the possible contribution of light scattering resonance to R_2. The standard formalism for Raman scattering intensity is described by three processes: (1) absorption of an incident photon that excites an electron, (2) interaction between the excited electron with a vibrational mode (or phonons in crystals), and (3) relaxation of the excited electron to the ground state, accompanied by the emission of a Raman photon as scattered light. For the Stokes Raman scattering process, the intensity of normal Raman scattering can be written as[10,56]:

$$I(E_L) = K\left|\frac{\langle f|H_{e-r}|b\rangle\langle b|H_{e-vib}|a\rangle\langle a|H_{e-r}|i\rangle}{(E_L - E_g - i\Gamma_a)(E_L - E_g - E_{vib} - i\Gamma_b)}\right|^2 \quad (1)$$

where $|i\rangle$, $|a\rangle$, $|b\rangle$, $|f\rangle$ are the initial, two intermediate, and final states, respectively; H_{e-r} and H_{e-vib} are the matrix elements for the Hamiltonian of light radiation and electron-vibration coupling, respectively; E_L is the energy of incident light, E_g is the energy of the electron transition, E_{vib} is the energy of the vibrational mode; Γ_a and Γ_b are damping parameters associated with the lifetime of the two intermediate states, $|a\rangle$ and $|b\rangle$, respectively. From the denominator in Eq. 1, there are two instances where maximum Raman intensity can be achieved. The first occurs when $E_L = E_g$, which corresponds to the incident light resonance, where the energy provided by the incident light excites an electron from the ground to an excited state. The second case, $E_L = E_g + E_{vib}$, occurs when the energy of the incident light matches that of the scattered light. We consider the possibility of R_2 stemming from scattered light resonance, as observed previously in REPs of copper phthalocyanine molecules on graphene[10]. The scattered light resonance for $\nu_{613} = 0.08$eV ($\mu_{Rh6G} = 2.33$ eV) occurs at 2.41 eV. Likewise, for $\nu_{1361} = 0.17$eV scattered light resonance is expected at 2.50 eV, and for $\nu_{1650} = 0.20$eV, it is expected at 2.53 eV. Evidently, scattered light resonance is mode-dependent, and the resonance peak position shifts accordingly. However, such mode-dependent effect is not observed in the Rh 6G/SnS_2 system, as all Rh 6G REPs show R_2 at 2.54 eV position, suggesting scattered light resonance is not the origin for R_2.

Second, in the theory of enhanced Raman scattering on semiconductors[12], charge-transfer (CT) resonances occur between substrate and adsorbate through intensity borrowing from vibronically coupled states. The band alignment diagram in Fig. 1a shows Rh 6G has the lowest unoccupied molecular orbital (LUMO) at −3.4 eV and the highest occupied molecular orbital (HOMO) at −5.7 eV, while the conduction band minimum (CBM) and valence band maximum (VBM) of SnS_2 are at around −5.0 and −7.3 eV, respectively[50,57,58]. In addition to molecular and exciton resonances, charge-transfer resonances are expected to occur from the SnS_2 VB to the Rh 6G LUMO at 3.8 eV and from the Rh 6G HOMO to the SnS_2 CB at 0.7 eV— which indicates a much lower excitation energy could be used to achieve direct charge-transfer resonance. Nevertheless, because these energies are far outside our excitation window, we do not believe R_2 originates from photo-induced CT.

Third, we consider an electronic hybridization concept proposed by Morton and Jensen[59], in which hybridization occurs between the molecule and substrate electronic states. To this end, we further measure the Rh 6G REPs on 2D MoS_2 and WSe_2 where Raman enhancement has been reported[2,5,60–64]

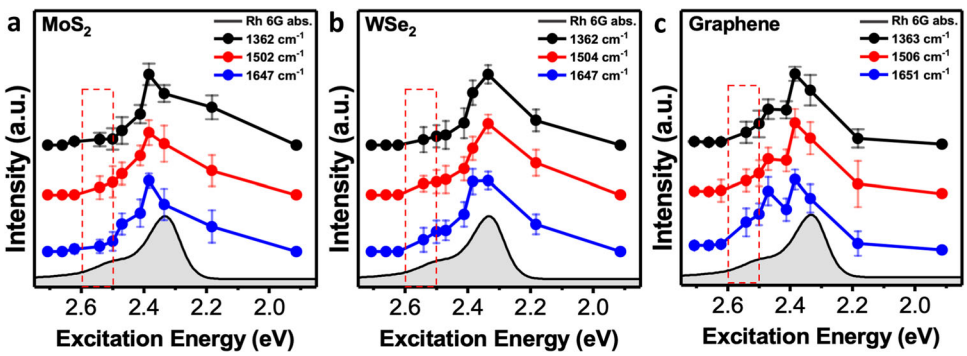

Fig. 3 REPs for Rh 6G deposited on different 2D materials. REPs for selected vibrational modes of Rh 6G deposited on MoS_2 (**a**), WSe_2 (**b**), and graphene (**c**). The absorption spectrum of Rh 6G is shown in each plot for comparison. The red dash rectangular labeled regions correspond to the R_2 region. Error bars represent the standard deviation from measuring multiple samples.

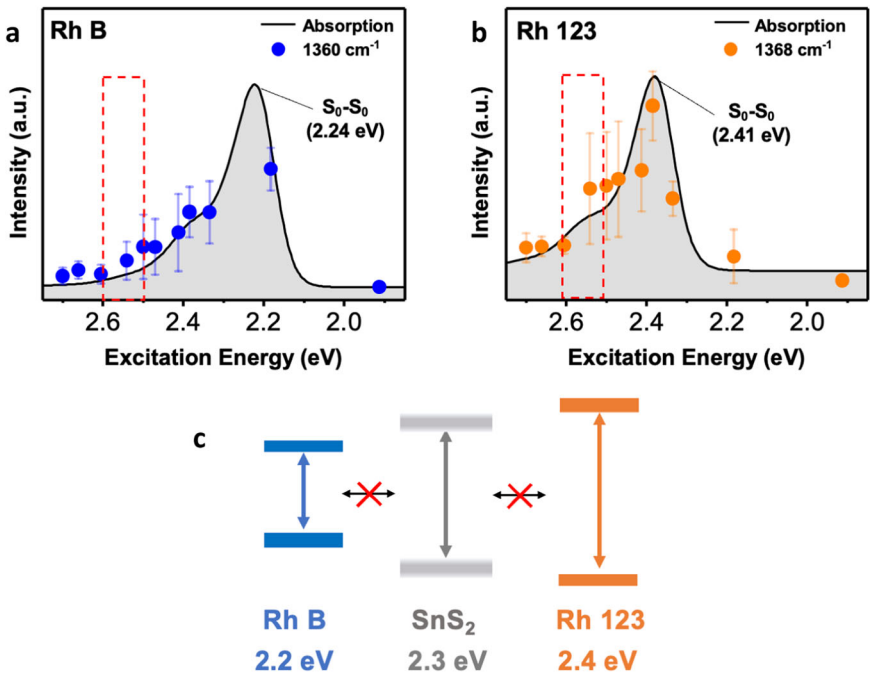

Fig. 4 Modulating exciton degeneracy in rhodamine/SnS_2. **a** The REP of 1360 cm^{-1} mode from Rh B/SnS_2. Note no feature at 2.5 eV is observed. **b** The REP of the 1368 cm^{-1} mode from Rh 123/SnS_2. The absorption spectra of Rh B and Rh 123 are shown in (**a**) and (**b**), respectively, for comparison. The red dash rectangular labeled regions in (**a**) and (**b**) correspond to the R_2 region. Error bars represent the standard deviation from measuring multiple samples. **c** Illustration showing exciton hybridization between SnS_2 and Rh B or Rh 123 does not occur due to exciton energy misalignment.

and that have electronic states close to either HOMO or LUMO of Rh 6G. For example, the MoS_2 VBM lies near the Rh 6G HOMO at −5.8 eV, while the WSe_2 VBM lies near the Rh 6G LUMO at −3.6 eV[65,66]. Figure 3a shows the Rh 6G/MoS_2 REPs overlaid on the Rh 6G absorption spectrum and scaled for better comparison, where the maximum occurs at 2.38 eV, matching well with the $S_{0,0}$-$S_{1,0}$ transition energy. Notably absent, however, is a resonance peak at 2.54 eV. Similarly, for Rh 6G/WSe_2 shown in Fig. 3b, the REPs also display a maximum at 2.33 eV, corresponding to the $S_{0,0}$-$S_{1,0}$ transition, and no secondary peak is observed. These results suggest that electronic hybridization is not responsible for R_2, although it may contribute to the Raman enhancement for the $S_{0,0}$-$S_{1,0}$ transition (around 2.35 eV excitation), as observed in the literature[59].

Moreover, we also measured the Rh 6G REPs on graphene, a semi-metal that does not possess a bandgap[67], and exciton hybridization is not expected. However, graphene has been demonstrated to enhance the Rh 6G signals by efficient charge transfers that prevent the recombination of electrons and holes in Rh 6G and lead to the suppression of the fluorescence[68,69], which allows us to obtain the REPs for Rh 6G. The Rh 6G/graphene REPs shown in Fig. 3c display a main peak at 2.38 eV, which is similar to that in other REPs discussed above. In addition, a shoulder peak is also observed at 2.47 eV, which matches well with the energy of the $S_{0,0}$-$S_{1,1}$ transition (i.e., 2.44 eV) measured from the shoulder peak in the absorption spectra (Fig. 1d). Of particular note, the energy of this shoulder peak (i.e., 2.47 eV) in the Rh 6G/graphene REPs is different from the energy of the R_2 peak (i.e., 2.54 eV) in Rh 6G/SnS_2 system. Notably, the R_2 peak blueshifts by about 0.1 eV, and we attribute it to exciton hybridization between the Rh 6G $S_{0,0}$-$S_{1,0}$ transition and the exciton in SnS_2. Spectra for Rh 6G on MoS_2, WSe_2, and graphene under various excitations are shown in Supplementary Fig. 7.

Modulation of molecular exciton degeneracy with SnS_2 exciton

The exciton hybridization in Rh 6G/SnS_2 system is further confirmed by measuring REPs on SnS_2 for molecules with different HOMO-LUMO gaps, i.e., $\mu_{mol} \neq \mu_{SnS_2}$. Particularly, Rh B and Rh 123 share the same xanthene core structure as Rh 6G but have different μ_{mol}, which allows adjustment of the degeneracy with μ_{SnS_2} in the rhodamine/SnS_2 complex. The typical Raman spectra for the two rhodamines deposited on SnS_2 are shown in Supplementary Fig. 8, where discernible xanthene ring bands are observed between 1190 and 1650 cm^{-1} for all, due to the same xanthene core structure. The slight differences in the lower frequency portion of the spectra are due to the vibrational modes related to different functional groups. The vibrational assignments are given in Supplementary Table 1.

The absorption spectrum for Rh B in Fig. 4a shows the characteristic $S_{0,0}$-$S_{1,0}$ ($\mu_{Rh\,B}$) and $S_{0,0}$-$S_{1,1}$ transitions at 2.24 and 2.34 eV, respectively. Because $\mu_{RhB} < \mu_{SnS_2}$, hybridization in Rh B/SnS_2 is not expected. In fact, the REP of the 1360 cm^{-1} mode of Rh B closely follows the absorption spectrum, and no feature at the R_2 energy is present, nor is a shift in the $S_{0,0}$-$S_{1,1}$ observed. Similarly, for Rh 123, the absorption spectrum in Fig. 4b shows the $S_{0,0}$-$S_{1,0}$ (μ_{Rh123}) and $S_{0,0}$-$S_{1,1}$ occur at 2.41 and 2.54 eV, respectively. Hybridization is again not expected since $\mu_{Rh123} > \mu_{SnS_2}$. Consequently, the REP for the 1368 cm^{-1} mode of Rh 123 shows a maximum at 2.41 eV and a small feature at ~2.5 eV, matching very well with the $S_{0,0}$-$S_{1,0}$ and $S_{0,0}$-$S_{1,1}$ transitions of Rh 123, respectively. Similar trends are observed for other xanthene ring modes (e.g., 1510 and 1647 cm^{-1} modes, Supplementary Fig. 9) in both Rh B and Rh 123. Importantly, in both rhodamine cases, there are no apparent shifts when comparing the peaks in the REPs and their absorption spectra, which is different from the case of Rh 6G. The diagram in Fig. 4c summarizes the exciton degeneracy for Rh B/SnS_2 and Rh 123/SnS_2, illustrating that the exciton hybridization does not occur. Therefore, for all three rhodamine analogs, only in

the Rh 6G/SnS_2 case, where the $\mu_{Rh6G} \cong \mu_{SnS_2}$ and hybridization is possible, a new resonance peak appears in the REP. The results clearly show that exciton hybridization occurs and plays an important role in Raman enhancement.

DISCUSSION

In summary, we perform a comprehensive investigation on the Raman enhancement effect of rhodamine molecules on 2D materials using excitation-dependent Raman spectroscopy measurements. The result suggests that degenerate excitons in Rh 6G and SnS_2 lead to strong coupling between them, causing an exciton hybridization. Particularly, compared to other systems without proper exciton alignment and no exciton hybridization is expected (e.g., Rh 6G/MoS_2, Rh 6G/WSe_2, and Rh 6G/graphene), the hybridization in Rh 6G/SnS_2 system leads to the observation of a new resonance peak at 2.54 eV (R_2) in the REPs. The exciton hybridization concept is further verified by measuring Rh B and Rh 123 REPs on SnS_2, which have μ_{mol} different from μ_{SnS_2}, and hybridization is not observed. This control experiment underscores the significance of precise exciton alignment. While exciton resonance with SnS_2 can be achieved under 2.33 eV excitation, the excitons from Rh B and Rh 123 fail to hybridize with SnS_2 due to misaligned energies. In instances where both molecular and exciton resonances are congruent—as in the Rh 6G/SnS_2 case, hybridization occurs, and is evidenced by the emergence of a new resonance peak in the REP. Lastly, we interpret the unusually intense C–C–C ring in-plane bending mode (613 cm^{-1}, Fig. 1b) under 2.33 eV as a consequence of the strong coupling—enabled by the exciton hybridization—which allows an excellent LOD of 10^{-13} M to be achieved. This LOD is comparable to plasmon-enhanced Raman spectroscopy and highlights the importance of efficient coupling between substrate and adsorbate. Although lower LOD was reported on other pristine 2D materials (e.g. TaS_2, $NbSe_2$, and 1T′ WSe_2)[44,46,47], we envision improved LOD to a similar level could be realized by leveraging our understanding on exciton resonance in Raman enhancement effect. For example, by tailoring the crystal structure of SnS_2 through defect, strain, and heterostructure engineering, one can change the band alignment with Rh 6G and consequently the exciton coupling strength, leading to even higher detection sensitivity. The present work provides important guidance to the rational design of future SERS substrates for trace-level detection based on exciton hybridization.

METHODS

Preparation of 2D materials

The bulk crystals of SnS_2, MoS_2, WSe_2, and graphene were purchased from HQ Graphene. The 2D materials were prepared via mechanical exfoliation and transferred onto cleaned 300 nm SiO_2/Si substrates.

Atomic force microscopy

The number of layers of SnS_2 was determined by atomic force microscopy (Bruker Dimension 3000) using the tapping mode.

Deposition of probe molecules

Rhodamine 6G (Sigma-Aldrich), Rhodamine B (Sigma-Aldrich), and Rhodamine 123 (Sigma-Aldrich) were dissolved in isopropyl alcohol (IPA) to make 10^{-4} M stock solutions (10 mL). Exfoliated 2D crystals were then submerged in the solution for 2 h and washed several times with IPA to remove excess molecules. For concentration-dependent studies, Rh 6G solutions, ranging from 10^{-4} to 10^{-14} M, were prepared by serial dilutions from the stock. After soaking for 2 h in the lowest concentration and washing, Raman spectra were acquired, and the sample was dipped in the next higher concentration and so on until the maximum concentration.

Optical measurements

Raman scattering measurements were carried out on a micro-Raman spectrometer (Horiba-JY T64000) in the triple-grating mode equipped with an 1800 g mm^{-1} grating. Signals were collected through a ×100 objective, and the power was kept <1 mW at the sample with an acquisition time of 60 s. Excitation-dependent Raman scattering measurements were performed with a series of laser lines from a Kr^+/Ar^+ ion laser (Coherent Innova 70C Spectrum), ranging from 458 to 647 nm. Micro-absorption measurements were performed in a custom-built setup, where reflectance and transmittance spectra were collected. Optical absorption of 10^{-5} M Rh 6G, Rh B, and Rh 123 solutions were carried out on a UV-vis spectrophotometer (Agilent CARY 5000). The X-ray photoelectron spectroscopy measurements were carried out on an integrated X-ray system (Thermo Scientific, Nexsa G2).

DATA AVAILABILITY

All data needed to evaluate the conclusions in the paper are present in the paper and the Supplementary Materials. The dataset analyzed in the current work is also available from the corresponding author upon reasonable request.

Received: 12 June 2023; Accepted: 18 January 2024;
Published online: 14 February 2024

REFERENCES

1. Ling, X. et al. Can graphene be used as a substrate for Raman enhancement? *Nano Lett.* **10**, 553–561 (2010).
2. Ling, X. et al. Raman enhancement effect on two-dimensional layered materials: graphene, h-BN and MoS_2. *Nano Lett.* **14**, 3033–3040 (2014).
3. Cai, Q. et al. Boron nitride nanosheets as improved and reusable substrates for gold nanoparticles enabled surface enhanced Raman spectroscopy. *Phys. Chem. Chem. Phys.* **17**, 7761–7766 (2015).
4. Lin, J. et al. Enhanced Raman scattering on in-plane anisotropic layered materials. *J. Am. Chem. Soc.* **137**, 15511–15517 (2015).
5. Kitadai, H., Wang, X., Mao, N., Huang, S. & Ling, X. Enhanced Raman scattering on nine 2D van der Waals materials. *J. Phys. Chem. Lett.* **10**, 3043–3050 (2019).
6. Muehlethaler, C. et al. Ultrahigh Raman enhancement on monolayer MoS_2. *ACS Photonics* **3**, 1164–1169 (2016).
7. He, Z. et al. Two-dimensional TiVC solid-solution MXene as surface-enhanced Raman scattering substrate. *ACS Nano* **16**, 4072–4083 (2022).
8. Karthick Kannan, P., Shankar, P., Blackman, C. & Chung, C.-H. Recent advances in 2D inorganic nanomaterials for SERS sensing. *Adv. Mater.* **31**, 1803432 (2019).
9. Yin, Z. et al. Recent progress on two-dimensional layered materials for surface enhanced Raman spectroscopy and their applications. *Mater. Today Phys.* **18**, 100378 (2021).
10. Ling, X., Moura, L. G., Pimenta, M. A. & Zhang, J. Charge-transfer mechanism in graphene-enhanced Raman scattering. *J. Phys. Chem. C* **116**, 25112–25118 (2012).
11. Amsterdam, S. H. et al. Electronic coupling in metallophthalocyanine-transition metal dichalcogenide mixed-dimensional heterojunctions. *ACS Nano* **13**, 4183–4190 (2019).
12. Lombardi, J. R. & Birke, R. L. Theory of surface-enhanced Raman scattering in semiconductors. *J. Phys. Chem. C* **118**, 11120–11130 (2014).
13. Yang, L. et al. A novel ultra-sensitive semiconductor SERS substrate boosted by the coupled resonance effect. *Adv. Sci.* **6**, 1900310 (2019).
14. Kim, J. et al. Quantum confinement induced excitonic mechanism in zinc-oxide-nanowalled microrod arrays for UV–Vis surface-enhanced Raman scattering. *J. Phys. Chem. C* **123**, 24957–24962 (2019).
15. Liu, Y., Gao, Z., Chen, M., Tan, Y. & Chen, F. Enhanced Raman scattering of CuPc films on imperfect WSe_2 monolayer correlated to exciton and charge-transfer resonances. *Adv. Funct. Mater.* **28**, 1805710 (2018).
16. Muccianti, C. et al. Coupled 2D semiconductor—molecular excitons with enhanced Raman scattering. *J. Phys. Chem. C* **124**, 27637–27644 (2020).
17. Huang, Y. et al. Tin disulfide—an emerging layered metal dichalcogenide semiconductor: materials properties and device characteristics. *ACS Nano* **8**, 10743–10755 (2014).

18. Shafique, A., Samad, A. & Shin, Y. H. Ultra low lattice thermal conductivity and high carrier mobility of monolayer SnS2 and $SnSe_2$: a first principles study. *Phys. Chem. Chem. Phys.* **19**, 20677–20683 (2017).
19. Sharma, K. et al. Strategies and perspectives of tailored SnS_2 photocatalyst for solar driven energy applications. *Sol. Energy* **231**, 546–565 (2022).
20. Zhou, X., Zhang, Q., Gan, L., Li, H. & Zhai, T. Large-size growth of ultrathin SnS_2 nanosheets and high performance for phototransistors. *Adv. Funct. Mater.* **26**, 4405–4413 (2016).
21. Huang, Y. et al. Highly sensitive and fast phototransistor based on large size CVD-grown SnS_2 nanosheets. *Nanoscale* **7**, 14093–14099 (2015).
22. Christoforidis, K. C., Sengele, A., Keller, V. & Keller, N. Single-step synthesis of SnS_2 nanosheet-decorated TiO_2 anatase nanofibers as efficient photocatalysts for the degradation of gas-phase diethylsulfide. *ACS Appl. Mater. Interfaces* **7**, 19324–19334 (2015).
23. Cui, X., Xu, W., Xie, Z. & Wang, Y. High-performance dye-sensitized solar cells based on Ag-doped SnS_2 counter electrodes. *J. Mater. Chem. A* **4**, 1908–1914 (2016).
24. Peng, Y. et al. Identifying infectiousness of SARS-CoV-2 by ultra-sensitive SnS_2 SERS biosensors with capillary effect. *Matter* **5**, 694–709 (2022).
25. Kamali, K. U. V. excited enhanced Raman scattering on carbon-doped SnS_2 nanoflowers. *Mater. Res. Bull.* **150**, 111757 (2022).
26. Li, F. et al. Semiconductor SERS on colourful substrates with Fabry–Pérot cavities. *Angew. Chem. Int. Ed.* **135**, e202218055 (2023).
27. Peter, L. M. Towards sustainable photovoltaics: the search for new materials. *Philos. Trans. R. Soc. A* **369**, 1840–1856 (2011).
28. Alessandri, I. & Lombardi, J. R. Enhanced Raman scattering with dielectrics. *Chem. Rev.* **116**, 14921–14981 (2016).
29. Lombardi, J. R. & Birke, R. L. A unified approach to surface-enhanced Raman spectroscopy. *J. Phys. Chem. C* **112**, 5605–5617 (2008).
30. Lombardi, J. R. & Birke, R. L. A unified view of surface-enhanced Raman scattering. *Acc. Chem. Res.* **42**, 734–742 (2009).
31. Williams, R. H., Murray, R. B., Govan, D. W., Thomas, J. M. & Evans, E. L. Band structure and photoemission studies of sns2and snse2: I. Experimental. *J. Phys. C: Solid State Phys.* **6**, 3631 (1973).
32. Burton, L. A. et al. Electronic and optical properties of single crystal SnS_2: an earth-abundant disulfide photocatalyst. *J. Mater. Chem. A* **4**, 1312–1318 (2016).
33. Skelton, J. M. et al. Lattice dynamics of the tin sulphides SnS_2, SnS and Sn_2S_3: vibrational spectra and thermal transport. *Phys. Chem. Chem. Phys.* **19**, 12452–12465 (2017).
34. Rusu, E. V., Syrbu, N. N., Tiron, A. V. & Zalamai, V. V. Band structure and optical constants of SnS_2 single crystals. *Mater. Res. Express* **6**, 046203 (2019).
35. Sriv, T., Kim, K. & Cheong, H. Low-frequency Raman spectroscopy of few-layer 2H-SnS_2. *Sci. Rep.* **8**, 2–8 (2018).
36. Hildebrandt, P. & Stockburger, M. Surface-enhanced resonance Raman spectroscopy of rhodamine 6G adsorbed on colloidal silver. *J. Phys. Chem.* **88**, 5935–5944 (1984).
37. Shim, S., Stuart, C. M. & Mathies, R. A. Resonance Raman cross-sections and vibronic analysis of rhodamine 6G from broadband stimulated Raman spectroscopy. *ChemPhysChem* **9**, 697–699 (2008).
38. Albrecht, A. C. & Hutley, M. C. On the dependence of vibrational Raman intensity on the wavelength of incident light. *J. Chem. Phys* **55**, 4438–4443 (1979).
39. Tang, J. & Albrecht, A. C. in *Raman Spectroscopy: Theory and Practice* 33–68 (Springer, 1970).
40. Long, D. A. *The Raman Effect: A Unified Treatment of the Theory of Raman Scattering by Molecules* Vol. 8 (John Wiley & Sons Ltd, 2002).
41. Warshel, A. Interpretation of resonance Raman spectra of biological molecules. *Annu. Rev. Biophys. Bioeng.* **6**, 273–300 (1977).
42. Watanabe, H., Hayazawa, N., Inouye, Y. & Kawata, S. DFT vibrational calculations of Rhodamine 6G adsorbed on silver: analysis of tip-enhanced Raman spectroscopy. *J. Phys. Chem. B* **109**, 5012–5020 (2005).
43. Jensen, L. & Schatz, G. C. Resonance Raman scattering of rhodamine 6G as calculated using time-dependent density functional theory. *J. Phys. Chem. A* **110**, 5973–5977 (2006).
44. Tao, L. et al. 1T′ transition metal telluride atomic layers for plasmon-free SERS at femtomolar levels. *J. Am. Chem. Soc.* **140**, 8696–8704 (2018).
45. Herzberg, G. & Teller, E. *Schwingungsstruktur der Elektronenübergänge bei mehratomigen Molekülen* Vol. 21B, 410–446 (1933).
46. Ekoya, B. G. M. et al. 2H Tantalum disulfide nanosheets as substrates for ultrasensitive SERS-based sensing. *ACS Appl. Nano Mater.* **5**, 8913–8920 (2022).
47. Lv, Q. et al. Ultrasensitive molecular sensing of few-layer niobium diselenide. *J. Mater. Chem. A* **9**, 2725–2733 (2021).
48. Yan, X., Shi, H., Jia, P. & Sun, X. LSPR tunable Ag@PDMS SERS substrate for high sensitivity and uniformity detection of dye molecules. *Nanomaterials* **12**, 3894 (2022).
49. Liu, C. et al. SERS substrate with wettability difference for molecular self-concentrating detection. *Nanotechnology* **32**, 37 (2021).
50. Gonzalez, J. M. & Oleynik, I. I. Layer-dependent properties of SnS_2 and $SnSe_2$ two-dimensional materials. *Phys. Rev. B* **94**, 125443 (2016).
51. Ling, X. & Zhang, J. First-layer effect in graphene-enhanced Raman scattering. *Small* **6**, 2020–2025 (2010).
52. Braslavsky, S. E. *Glossary of Terms Used in Photochemistry*, 3rd edition (IUPAC Recommendations 2006) Vol. 79, 293–465 (2007).
53. Zhang, X. F. & Li, F. Interaction of graphene with excited and ground state rhodamine revealed by steady state and time resolved fluorescence. *J. Photochem. Photobiol. A* **246**, 8–15 (2012).
54. Dieringer, J. A. et al. Surface-enhanced Raman excitation spectroscopy of a single rhodamine 6G molecule. *J. Am. Chem. Soc.* **131**, 849–854 (2009).
55. Guthmuller, J. & Champagne, B. Resonance Raman spectra and Raman excitation profiles of rhodamine 6G from time-dependent density functional theory. *ChemPhysChem* **9**, 1667–1669 (2008).
56. Jorio, A., Saito, R., Dresselhaus, G. & Dresselhaus, M. in *Raman Spectroscopy in Graphene Related Systems* 103–119 (Wiley-VCH, 2011).
57. Whittles, T. J. et al. Band alignments, valence bands, and core levels in the tin sulfides SnS, SnS_2, and Sn_2S_3: experiment and theory. *Chem. Mater.* **28**, 3718–3726 (2016).
58. Burton, L. A. et al. Synthesis, characterization, and electronic structure of single-crystal SnS, Sn_2S_3, and SnS_2. *Chem. Mater.* **25**, 4908–4916 (2013).
59. Morton, S. M. & Jensen, L. Understanding the molecule-surface chemical coupling in SERS. *J. Am. Chem. Soc.* **131**, 4090–4098 (2009).
60. Sun, S. et al. Defect-rich monolayer MoS_2 as a universally enhanced substrate for surface-enhanced Raman scattering. *Nanomaterials* **12**, 896 (2022).
61. Lee, Y. et al. Enhanced Raman scattering of rhodamine 6G films on two-dimensional transition metal dichalcogenides correlated to photoinduced charge transfer. *Chem. Mater.* **28**, 180–187 (2016).
62. Majee, B. P., Mishra, S., Pandey, R. K., Prakash, R. & Mishra, A. K. Multifunctional few-layer MoS_2 for photodetection and surface-enhanced Raman spectroscopy application with ultrasensitive and repeatable detectability. *J. Phys. Chem. C* **123**, 18071–18078 (2019).
63. Lv, Q. et al. Femtomolar-level molecular sensing of monolayer tungsten diselenide induced by heteroatom doping with long-term stability. *Adv. Funct. Mater.* **32**, 2200273 (2022).
64. Ling, X. et al. Lighting up the Raman signal of molecules in the vicinity of graphene related materials. *Acc. Chem. Res.* **48**, 1862–1870 (2015).
65. Guo, Y. & Robertson, J. Band engineering in transition metal dichalcogenides: stacked versus lateral heterostructures. *Appl. Phys. Lett.* **108**, 233104 (2016).
66. Kang, J., Tongay, S., Zhou, J., Li, J. & Wu, J. Band offsets and heterostructures of two-dimensional semiconductors. *Appl. Phys. Lett.* **102**, 012111 (2013).
67. Castro Neto, A. H., Guinea, F., Peres, N. M. R., Novoselov, K. S. & Geim, A. K. The electronic properties of graphene. *Rev. Mod. Phys.* **81**, 109–162 (2009).
68. Xie, L., Ling, X., Fang, Y., Zhang, J. & Liu, Z. Graphene as a substrate to suppress fluorescence in resonance Raman spectroscopy. *J. Am. Chem. Soc.* **131**, 9890–9891 (2009).
69. Thrall, E. S., Crowther, A. C., Yu, Z. & Brus, L. E. R6G on graphene: high Raman detection sensitivity, yet decreased Raman cross-section. *Nano Lett.* **12**, 1571–1577 (2012).

ACKNOWLEDGEMENTS

This material is based upon work supported by the National Science Foundation (NSF) under Grant No. (1945364). Work by X.L. was supported by the U.S. Department of Energy (DOE), Office of Science, Basic Energy Sciences (BES) under Award DE-SC0021064. L.P. and X. L. acknowledge the support of the ACS Petroleum Research Fund under Award 61965-ND10. H.K. and X.L. acknowledge the valuable discussion from Prof. Lawrence Ziegler.

AUTHOR CONTRIBUTIONS

H.K. and X.L. conceived the project. H.K. and L.P. performed the optical spectroscopy experiments. H.K. and Q.T. prepared and characterized the exfoliated samples. H.K. and X.L. performed the analysis and interpretation of the data with input from L.P. and Q.T. H.K. and X.L. wrote the manuscript with contributions from all authors.

COMPETING INTERESTS

The authors declare no competing interests.

ADDITIONAL INFORMATION

Supplementary information The online version contains supplementary material available at https://doi.org/10.1038/s41699-024-00446-z.

Correspondence and requests for materials should be addressed to Xi Ling.

Reprints and permission information is available at http://www.nature.com/reprints

Publisher's note Springer Nature remains neutral with regard to jurisdictional claims in published maps and institutional affiliations.